Formation and stability of oxygen-rich bubbles that shape photosynthetic mats

T. BOSAK,[1] J. W. M. BUSH,[2] M. R. FLYNN,[3] B. LIANG,[1] S. ONO,[1] A. P. PETROFF[1] AND M. S. SIM[1]

[1]*EAPS, Massachusetts Institute of Technology, Cambridge, MA, USA*
[2]*Department of Applied Mathematics, MIT, Cambridge, MA, USA*
[3]*Department of Mechanical Engineering, University of Alberta, Edmonton, AB, Canada*

ABSTRACT

Gas release in photic-zone microbialites can lead to preservable morphological biosignatures. Here, we investigate the formation and stability of oxygen-rich bubbles enmeshed by filamentous cyanobacteria. Sub-millimetric and millimetric bubbles can be stable for weeks and even months. During this time, lithifying organic-rich laminae surrounding the bubbles can preserve the shape of bubbles. Cm-scale unstable bubbles support the growth of centimetric tubular towers with distinctly laminated mineralized walls. In environments that enable high photosynthetic rates, only small stable bubbles will be enclosed by a dense microbial mesh, while in deep waters extensive microbial mesh will cover even larger photosynthetic bubbles, increasing their preservation potential. Stable photosynthetic bubbles may be preserved as sub-millimeter and millimeter-diameter features with nearly circular cross-sections in the crests of some Proterozoic conical stromatolites, while centrimetric tubes formed around unstable bubbles provide a model for the formation of tubular carbonate microbialites that are not markedly depleted in ^{13}C.

INTRODUCTION

Modern microbial sedimentary structures provide examples of biological interactions with sediments on Earth since life's early beginnings (Noffke *et al.*, 2006; Schieber *et al.*, 2007; Bosak *et al.*, 2009). For example, the presence of organic-rich laminae that were rolled up, contorted or wrinkled due to desiccation, gas release or wave and current action in both modern and ancient sedimentary environments indicates that laminated sediments were bound by microbial filaments or biopolymers at the time of deformation (e.g. Demicco & Hardie, 1994; Gehling, 2000; Gerdes *et al.*, 2000; Schieber *et al.*, 2007; Bengtson *et al.*, 2009). Gases such as CO_2, CO, H_2, CH_4 and H_2S, produced by light-independent processes can deform the primary morphology of shallow- and deep-water microbialites, creating fenestrae, voids and gas domes (e.g. Gerdes *et al.*, 2000; Noffke *et al.*, 2001; Schieber *et al.*, 2007). Rather than investigating this secondary porosity, here we examine the development of the primary porosity caused by O_2-rich bubbles produced by cyanobacteria. We ask how photosynthetic bubbles shape growing mats, and examine the preservation potential of these shapes by lithification.

The release of O_2 by modern photosynthetic microbes is particularly noticeable in benthic environments where bubbles emerge from slimy films formed by cyanobacteria and other microbes on solid or liquid surfaces (Fig. 1A). Oxygen-rich bubbles form not only on the surface, but also within and under photosynthetic biofilms, creating blisters (Jorgensen *et al.*, 1983; Revsbech *et al.*, 1983) and adding buoyancy to vertical structures in the mat (Campbell & Golubic, 1985; Schultze-Lam *et al.*, 1996; McGregor & Rasmussen, 2008). When these mat-trapped bubbles are abundant, mats can detach from the underlying surface, spreading the floating microbial communities (Wilson, 1965; Golubic, 1973). Here, we focus on a different manifestation of photosynthetic O_2 production: bubbles that appear on the surface of the biofilm and remain attached (Fig. 1). When enmeshed by fast-gliding microbes, stable bubbles can give rise to protuberances ranging in diameter from sub-mm to about 2 mm, while even larger and unstable enmeshed bubbles give rise to organic-walled tubes. We identify environmental and biological conditions conducive to the stability of mat-attached bubbles by examining the formation and the preservation of gas-related morphologies in oxygenic mats, and by developing a supporting analytical model that builds upon related studies of
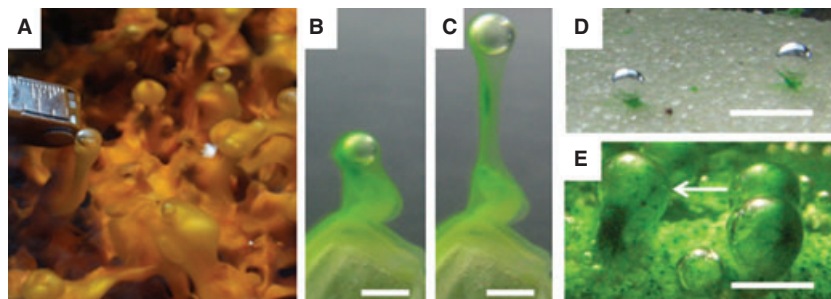
Fig. 1 Gas-related macroscopic morphologies in photosynthetic mats. (A) Bubble-capped towers in Yellowstone National Park (YNP). The smallest divisions on the scale are 1 mm. (B) Mat growth around a bubble in an enrichment culture of cyanobacteria from YNP in equilibrium with air. (C) The same field of view as in (B) after 2 h. (D) Bubbles attached to cyanobacterial biomass in a very young culture where most of the silica sand substrate was not covered by the mat. (E) Pattern formation (arrow pointing to dark dots) in the mesh covering bubbles depends on microbial motility. Scale bar in (B) and (C): 3 mm. Scale bar in (D) and (E): 5 mm.

underwater breathing by aquatic arthropods (Thorpe & Crisp, 1947; Flynn & Bush, 2008).

MATERIALS AND METHODS

Culturing media and growth conditions

Cyanobacterial mats were observed *in situ* in Sentinel Meadows and Fairy Creek in Yellowstone National Park (YNP) and the samples were collected under permit #YELL-2008-SCI-5758 from National Park Services. The bacteria were grown on solid substrate (agar, silica sand or aragonite sand) at 45 °C in modified Castenholz D medium (Castenholz, 1988) containing a lower concentration of nitrate and phosphate (2.3 mM NO_3^- and 0.8 mM PO_4^{3-}, respectively) at pH 7.6 and initially in equilibrium with an anaerobic atmosphere of 5% CO_2, 5% H_2 and 90% N_2. Alternatively, cone-forming cultures were incubated in the medium with the same composition, but equilibrated with air at pH 7.6. The cultures were incubated with a fluorescent cold light source on a 12-h day–night cycle. The medium was exchanged weekly. Lithification in the medium was promoted by lowering the phosphate concentration to 80 μM (with 0.23 mM NO_3^-), and by the addition of 35 mM $CaCl_2$ and 40 mM $MgCl_2$ to the final concentrations of 3.5 mM for calcium and 4 mM for magnesium, respectively. The sterile medium prepared in this manner initially did not contain $CaCO_3$ precipitate.

Microscopy

Samples were removed from actively growing cultures by a sterile surgical blade, fixed with 2.5% glutaraldehyde dissolved in 0.1 M sodium cacodylate buffer (pH 7.4) for 2 h. The fixative was washed away with 0.1 M sodium cacodylate, samples were embedded in Sakura TissueTek O.C.T. compound (VWR, West Chester, PA, USA), frozen for at least 2 h and

sectioned to a thickness of 10–50 μm using a cryo-stat (Leica, Wetzlar, Germany). These sections were washed with 0.1 M sodium cacodylate buffer to remove O.C.T. and imaged using a Zeiss Axio Imager M1 epifluorescence microscope or Zeiss LSM510 confocal microscope (Carl Zeiss, Thornwood, NY, USA) at the MIT W. M. Keck Microscopy Facility. Extra-cellular polymeric substances were stained by a 1:1 mixture of the solutions A and B. The solution A contained 10% w/v KOH in 10% v/v glycerol and the solution B contained 0.1% w/v Calcofluor White (Sigma-Aldrich, St. Louis, MO, USA), respectively (Hageage & Harrington, 1984). The sample was incubated at 45 °C for 5 min and subsequently rinsed with 0.1 M sodium cacodylate buffer. Chlorophyll autofluores-cence was imaged using excitation at 505 nm, emission at 615 nm and Calcofluor White fluorescence was imaged by Perkin Elmer spinning disc confocal microscope at the MIT W. M. Keck Microscopy Facility using excitation at 405/40 nm, and emission at 455 nm, respectively. Calcofluor White stains a number of polysaccharides including cellulose, pectin, chitin, carboxylated polysaccharides, beta-1,3-glucans and others (Hughes & McCully, 1975).

Mineral analysis

The mineralogy of precipitates in thin sections was confirmed by Raman spectroscopy. The Raman spectra were collected on a spectrometer excited by a 514.5 nm beam of an Ar/Kr mixed ion laser with a collection time of 3–10 min at the MIT Mineral Physics Lab. The diameter of the focus beam was <5 μm. Major peaks were assigned at Raman shift 1004 and 1156 cm^{-1} for cyanobacteria, 1085 cm^{-1} for calcium carbonate, and 1095 cm^{-1} for embedding O.C.T. The morphology and elemental composition of the precipitated minerals were examined by a low vacuum environmental scanning electron microscope coupled with energy dispersive X-ray analyser at a voltage of 5–10 kV and a magnification of 2000–10 000×. The microscope is suited for the viewing of uncoated samples.

Measurement of gas composition

The concentration of gases in the bubbles was determined by Shimadzu gas chromatograph GC-8A with a thermal conductivity detector at 60 mA, using a Molesieve 5A (60/80 mesh) column and Hayesep Q (80/100 mesh) columns. The injector temperature was 100 °C and the oven was at 80 °C with He as a carrier gas. Photosynthetic bubbles were sampled at least 3 h after the beginning of the daily light cycle. Bubbles that remained stable at night were sampled at least 4 h after the end of the light cycle. Gases were analyzed immediately after sampling. Oxygen fluxes from the mat surface were determined from at least three profiles of oxygen measured by microelectrodes in media equilibrated with atmospheric CO_2 or 5% CO_2, respectively.

RESULTS

Bubble-related morphologies in modern photosynthetic mats

Distinct morphological features develop around gas bubbles in actively photosynthesizing microbial mats in YNP and in our laboratory (Fig. 1). Most of the bubbles that develop within the mat range in scale from centimetric irregularly shaped blisters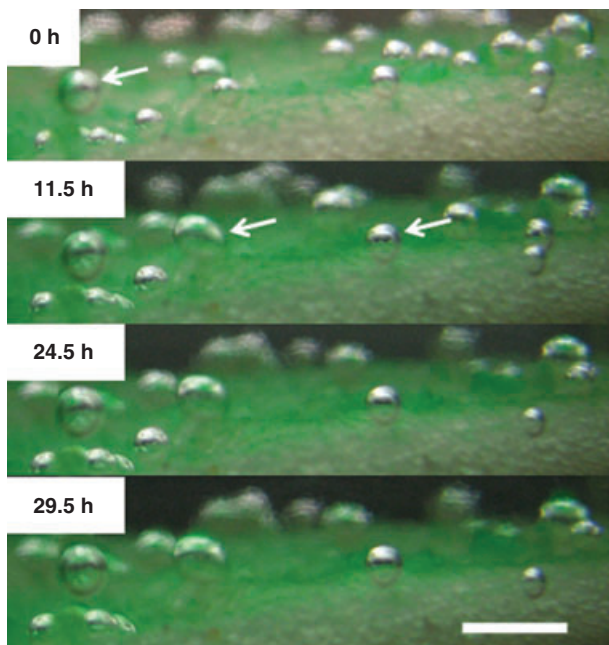 down to 10–100 μm diameter pores that are visible only in thin sections (Bosak et al., 2009). In contrast to the predominantly horizontal mat-trapped blisters, some mm-size bubbles develop at the topographic highs and can promote the growth of distinctly vertical structures in the mat (Figs 1, S1 and S2). The diameter and shape of these mat-attached bubbles can remain remarkably stable for days and even weeks (Figs 2 and S2). Because motile filamentous *Oscillatorean* cyanobacteria (McGregor & Rasmussen, 2008; Bosak et al., 2009) can colonize the gas–liquid interface (Figs 1 and S1), the growth of vertical structures cannot be attributed solely to the physical lifting of the mat by bubbles. Instead, the biomass on the surface of stable bubbles distributes itself dynamically, depending on various environmental factors that control the photosynthetic rate (Fig. 3).

Both mat-trapped and mat-attached bubbles contain a high concentration of O_2 relative to the overlying atmosphere (Table 1), indicating that the main source of gas in the bubbles is oxygenic photosynthesis and not the release of non-photosynthetic gases. In media incubated under an anaerobic atmosphere containing 5% CO_2, 5% H_2 and 90% N_2 (to a total of 10^5 Pa), bubbles nucleate when the oxygen concentration

Fig. 2 Stable photosynthetic bubbles at the surface of a thin cyanobacterial biofilm (green). These bubbles retain their size and position for at least 29.5 h even in the dark. 0 h denotes the beginning of the sequence of photographs, and photographs were taken every 0.5 h for 29.5 h (only 11.5, 24.5 and 29.5 h snapshots are shown). The culture was kept in the dark between 12.5 and 24.5 h. Scale bar: 5 mm (relative to the bubbles in the front).
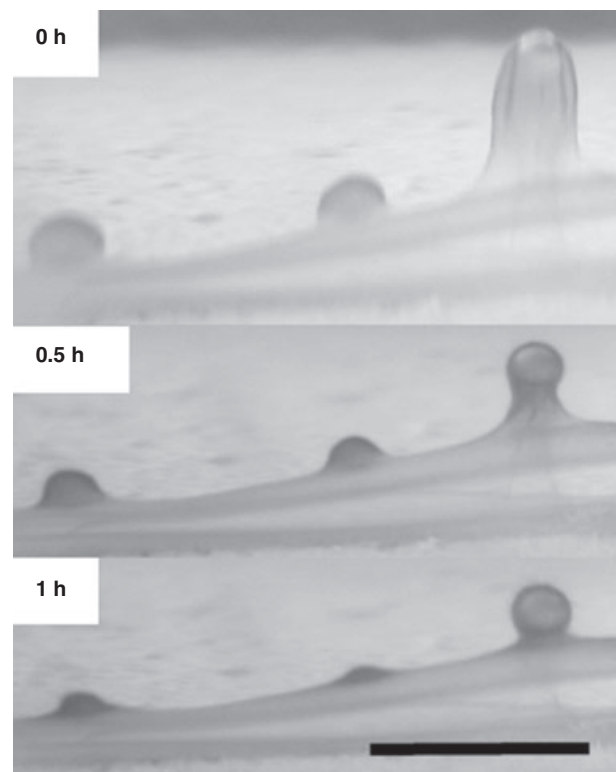

Fig. 3 Response of the microbial mesh around bubbles to a decrease of the light intensity from 30 to 10 μE m^{-2} s^{-1}. 0 h denotes the time after the change of light intensity. Snapshots of the same field of view at 10 μE m^{-2} s^{-1} were taken after 0.5 and 1 h. The rightmost bubble is surrounded by a thin microbial mesh at the high light intensity and retains nearly the same radius at a lower light intensity because it is surrounded by a thicker microbial mesh. Scale bar: 5 mm.

Table 1 Gas composition of mat-attached and mat-trapped bubbles (expressed as a molar ratio of O_2/N_2 or CO_2/N_2). The dashes denote values below the detection limit (2 μM for O_2 and 1.6 μM for CO_2 in 50 μL of the analyzed gas). Bubbles did not contain any detectable H_2, CO or CH_4

	Molar ratio	
Sample	O_2/N_2	CO_2/N_2
Anaerobic atmosphere mat-attached	–	0.056
bubble (night)	0.067	0.017
Mat-attached bubble (day)	0.237	–
	0.229	–
	0.277	0.005
	0.323	0.004
Large mat-trapped bubble	0.861	–
	0.962	–
	1.271	–
	1.557	–

close to the biomass is about 200 μM. This oxygen concentration exceeds that predicted by the equilibrium with an atmosphere containing 21% O_2 at 10^5 Pa at 45 °C (i.e. air). The number of mat-attached bubbles decreases after the daily onset of a 12-h dark cycle but some mat-attached bubbles persist throughout the dark cycle (Figs 2 and S2), indicating that other gases can replace oxygen and maintain the pressure in the bubble. Our measurements of gas composition in the bubbles after the dark incubation suggest that these other gases are most likely N_2 and CO_2 (Table 1). Similar phenomenon was observed previously in persistent mat-trapped blisters (Jorgensen *et al.*, 1983; Revsbech *et al.*, 1983). Locally elevated concentration of oxygen in microbial mats thus promotes the nucleation of bubbles. Once formed, these stable bubbles are able to persist and maintain their submillimetric to millimetric radii over the diurnal cycle. The model outlined in the Appendix addresses the relationship between the density of bacterial film and the expected size of stable bubbles in water of prescribed dissolved gas concentration.

In addition to small, nearly spherical stable bubbles, less spherical and only partially covered bubbles can attain cm-scale diameters and heights within a couple of hours (Figs 4, S2 and S3). These unstable bubbles determine the initial radius of gas conduits that grow rapidly upward, bend, pinch, swell and coalesce (Fig. 4). The nearly vertical microbial mesh surrounding the conduits thickens outward due to microbial growth, much like a horizontal surface of a mat would, and

inward, if the supply of the gas from the underlying mat ceases. This thickening occurs within several days to weeks. Small mat-covered blisters also develop on the sides of tubes (Fig. 4C). Cm-diameter tubes and large unstable partly covered bubbles form primarily in solutions where inorganic carbon is abundant. In our experimental system, bubbles with diameters exceeding one centimeter form only in the medium initially equilibrated with 5% CO_2 and 0% O_2 in the atmosphere, whereas only smaller bubbles form in the medium is initially equilibrated with air (0.04% CO_2 and 20% O_2). The development of large unstable bubbles may be a consequence of a 50% higher flux of oxygen from the mats into the medium under high-DIC conditions.

Recognition and preservation of bubble-like morphologies in mats

The recognition of gas-related morphologies in fossil microbialites requires not only that bubbles form and remain attached to the mat, but also that the mat around them be preserved by lithification. In our laboratory cultures, syngenetic precipitation of non-equant high-Mg calcite crystals smaller than 5 μm within the dense bubble-enclosing biomass (Fig. 5) enables the preservation of gas-related morphologies. The minerals nucleate primarily in the regions rich in extracellular polymeric substances (Fig. S4), but do not encrust cyanobacterial filaments. Under our experimental conditions, regions that formerly contained gas bubbles remain empty, but in fossil microbialites, they will likely be filled in by later cements.

Vertical cross-sections of cones, tubes and towers grown in lithifying laboratory cultures reveal the presence of 20- to 150-μm-thin dark, dense laminae separated by 0.1- to 1-mm-thick lighter regions containing porously arranged filaments or coccoidal cyanobacteria (Figs 5 and S4). Former bubbles are recognizable as circular or irregularly shaped empty spaces enclosed by dark dense laminae (Figs 5 and S4). Because 100 μm-1 mm diameter bubbles form mainly at the topographic highs (Bosak *et al.*, 2009), empty circular regions with sub-mm diameters and surrounded by microbial filaments are primarily found in the center of conical stromatolites in hot springs and cones that form in laboratory cultures (Jones *et al.*, 1998; Stueeken *et al.*, 2008; Bosak *et al.*, 2009).

The internal morphology of photosynthetic tubes that develop around unstable oxygen-rich bubbles reflects a
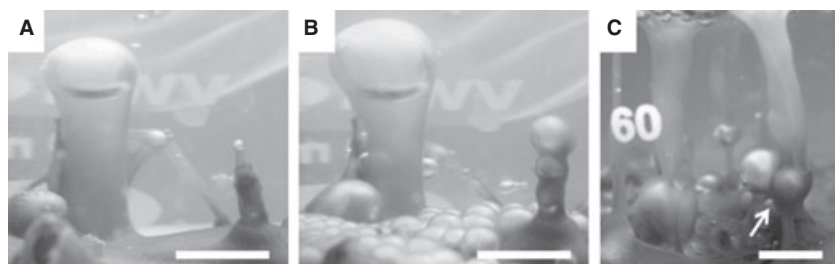

Fig. 4 Tubes forming around large, unstable photosynthetic bubbles. (A) One-day-old tube with a large, non-spherical bubble. (B) The same field of view after 5 h. (C) Denser, 1-week-old tubes. Arrow shows a pair of merged tubes. Photosynthetic bubbles often grow on the sides of tubes (right). Scale bar: 5 mm.
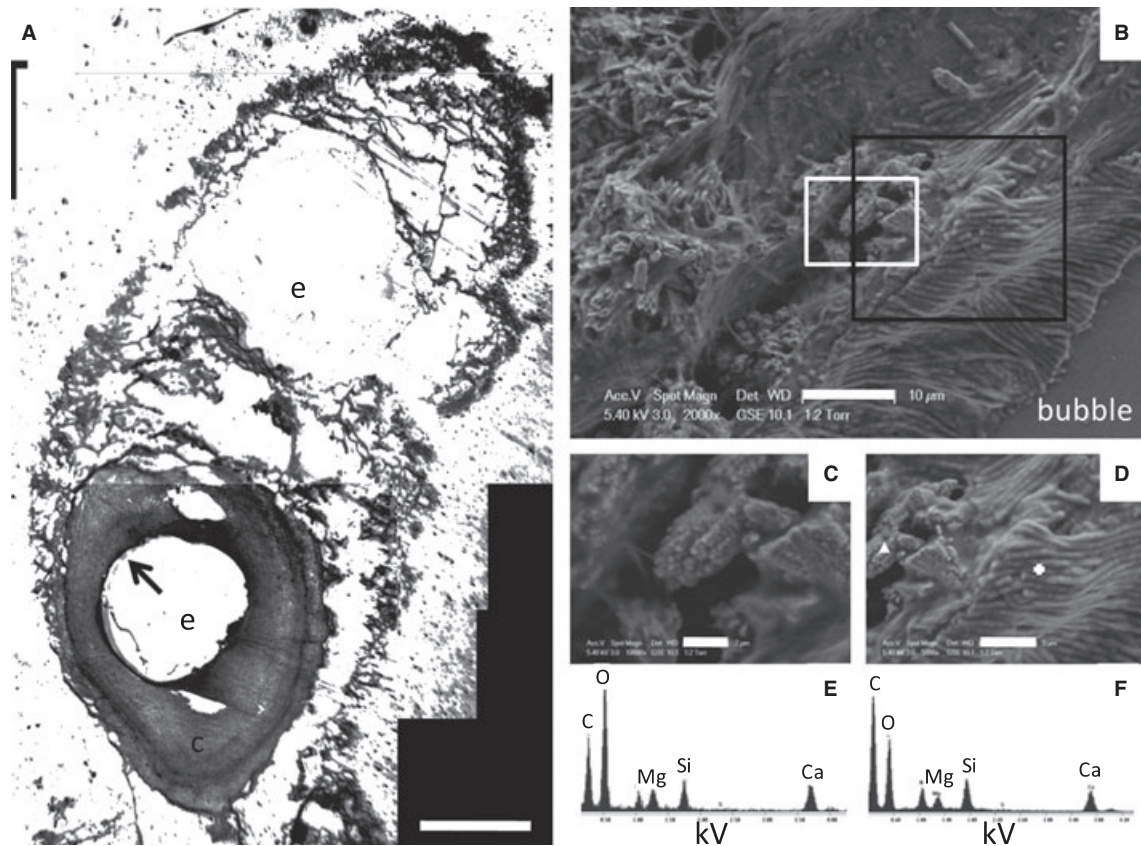
Fig. 5 Preservation of bubbles within microbial structures. (A) Transmitted light image (mosaic) of the vertical thin section of a microbial cone. A large bubble surrounded by multiple laminae is visible in the middle, another large bubble surrounded by discontinuous laminae is visible above (e). The darkest regions (e.g. arrow) contain calcium carbonate minerals. The thick lighter region (c) contains abundant coccoidal cyanobacteria. Scale bar: 2 mm. (B) Scanning electron micrograph of the filamentous cyanobacteria (black rectangle) immediately around the bubble and the adjacent mineral layer (white rectangle) in the area indicated by an arrow in (A). Scale bar: 10 μm. (C) Environmental scanning electron micrograph of minerals within the white rectangle in (B). Scale bar: 2 μm. (D) Environmental scanning electron micrograph of the region indicated by the black rectangle in (B). Scale bar: 5 μm. (E) Energy dispersive X-ray spectrum of the minerals marked by a triangle in (D). (F) Energy dispersive X-ray spectrum of the biomass marked by a cross in (D) indicating a lower amount of Ca, Mg and O in the biomass relative to the crystalline calcium carbonate. *X*-axis in E, F, stands for kV, *Y*-axis stands for counts.

combination of two main growth directions and rates. The initially porous mesh extends upward fast, creating tall vertical tubes (Fig. 4). The walls of the tubes subsequently undergo a slower lateral thickening visible as the succession of 0.5–1 mm wide, porous laminae and thinner, ~50–200 μm thick dense laminae (Fig. 6). The internal structure of the laminae is determined by the orientation of cyanobacterial filaments: the dense laminae contain primarily vertical and mutually aligned filaments (Fig. S4), and the porous laminae contain horizontal or randomly oriented filaments (Fig. S4). Because the number of laminae in the walls is smaller than the number of days or light periods spanning the growth and maturation of the tube samples, the lamination is not diurnal.

DISCUSSION

Bubbles on the surface of photosynthetic mats provide more surface area to cyanobacteria that live attached to surfaces, as is the case for cone and tube-forming cyanobacteria. Although mat-attached bubbles do not act as a significant reservoir of gaseous CO_2, they may enable microbes to access to higher concentrations of dissolved inorganic carbon or other nutrients in the upper portions of stratified solutions. For example, measurements of carbon fractionation in conical mats growing under the conditions of low flow in YNP indicate that these mats experience carbon limitation (Jahnke *et al.*, 2004). In this case, bacteria colonizing mat-attached or mat-trapped bubbles will be closer to the overlying nutrient source (either the atmosphere, or the top of a stratified water column).

Geobiological implications

Our analysis (Appendix) predicts that the volume of an individual photosynthetic bubble should decrease as more bacteria accumulate along the gas–water interface. Stable photosynthetic bubbles in shallow, well-illuminated water may be either large and lightly covered by cyanobacteria, or small and heavily covered. Conversely, stable bubbles that
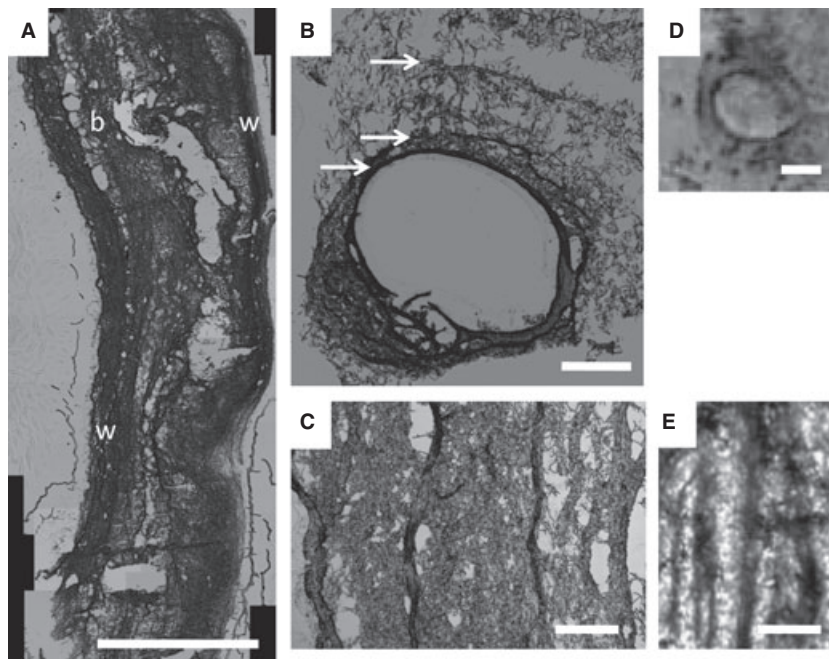
Fig. 6 Internal structure of photosynthetic tubes that grew around unstable bubbles. (A) Transmitted light micrograph (mosaic) of a vertical thin section through a cm-scale tube. The tube has densely laminated walls (w). Remnants of small bubbles are visible in the area marked by (b). The biomass in the interior of the tube grew after the gas release ceased. Scale bar: 5 mm. (B) Transmitted light micrograph (mosaic) of a horizontal thin section through a cm-scale tube [different sample than the one shown in (A)]. Arrows indicate thin dense laminae surrounding the central cavity. Dark laminae are partially lithified. Scale bar: 0.2 mm. (C) Transmitted light micrograph of the vertical laminae in the tube wall (vertical cross-section). Scale bar: 0.3 mm. (D) Polished hand sample of the Neoarchean tube (horizontal cross-section). Adapted from Murphy & Sumner (2008, Figure 6A). Scale bar: 1 cm. (E) Photomicrograph of the Neoarchean tube wall. Adapted from Murphy & Sumner (2008, Figure 8A). Scale bar: 0.3 mm.

emerge in deeper, less well-illuminated waters will persist only when they are inhabited by relatively dense biofilms and are relatively large in size. Similarly, when there is abundant dissolved gas (O_2, CO_2) in the medium, we might expect either lightly covered, large bubbles; moderately covered, medium-sized bubbles; or heavily covered small bubbles. These conclusions are not intuitive because large and small bubbles have different pressures and can therefore withstand different forces, hydrostatic or otherwise.

The density of the photosynthetic biofilm around bubbles determines the preservation potential and the size of gas-related morphologies in fossil microbialites. For example, our laboratory and field observations indicate that although mm-sized bubbles form at the surface of photosynthetic mats (Figs 1 and 3), they are incompletely covered by microbial mesh and are thus less likely to be preserved. On the other hand, heavily covered small stable bubbles in our lithifying laboratory cultures and modern conical stromatolites tend have diameters on the order of ∼100–200 μm and are best visible in thin sections (Jones *et al.*, 1998; Bosak *et al.*, 2009). Given that only small bubbles are expected to be covered by a dense, preservable mesh in shallow, well-illuminated modern hot springs, it is not surprising that only ∼100-μm-diameter circular features are preserved in lithified modern conical stromatolites. Examples of relatively uncovered bubbles also have been noted in pinnacled benthic microbial mats in the peren-

nially ice-covered Antarctic Lake Hoare at depths of up to 8 m in areas that are supersaturated with respect to O_2 (Vopel & Hawes, 2006). Because only snapshots of these mats exist, it remains unclear whether these bubbles are, in fact, steady. Much more heavily covered bubbles may nucleate in even deeper oxygenic pinnacled mats (Wharton *et al.*, 1983), but such bubbles have not been reported to date.

Former bubbles in fossil microbialites are recognizable as regions with a nearly circular cross-section enclosed by organic-rich laminae, such as those occurring in the central zone of a Proterozoic conical stromatolite (Donaldson, 1976). One hundred μm to mm-diameter circular regions attributed to fossil bubbles can also be identified within the mm-wide central zones of a number of other Proterozoic conical stromatolites (Bosak *et al.*, 2009). The diameters of bubbles that formed in relatively deep-water Proterozoic stromatolites (Donaldson, 1976; Hoffman, 1976) can be larger than those observed in modern stromatolites because almost all stable bubbles in relatively deep water would have been heavily covered and larger, owing to the greater stability of large bubbles at greater hydrostatic pressures (Appendix). Gas-induced contortions of microbial laminae in shallow-water microbialites may be considerably harder to recognize both because they are smaller than ∼100 μm, and because other forces including desiccation and wave action deform the laminae. Similarly, photosynthetic bubbles will not be pre-

served in environments with a low lithification potential and they will neither be distinct nor preserved in structures that harbor abundant secondary porosity caused by processes that degrade organic matter and destroy the primary lamination.

The larger scale morphology, internal textures and the distribution of fossil bubbles within the rock matrix enable the distinction between photosynthetic bubbles and bubbles lithified at the air–water interface in the absence of mats (Chafetz *et al.*, 1991; Fouke *et al.*, 2000). The latter bubbles are surrounded by a ∼100–200 μm thin mineral crust that consists of only two distinct mineral layers. The two layers are adjacent to one another and form nearly continuous thin sheets (Chafetz *et al.*, 1991; Fouke *et al.*, 2000). The thinness of these sheets and crusts is a consequence of rather brief accretion in the immediate proximity of the horizontal air–water interface. In contrast, present primarily at the topographic highs within thicker, taller, distinctly laminated conical or tubular structures, fossil photosynthetic bubbles bear evidence of repeated interactions between growing mats, gas and precipitating minerals that take place below the horizontal air–water interface.

The growth of nearly vertical tubular structures around oxygen-rich bubbles in our non-turbulent lithifying laboratory cultures provides a model for the growth of cm-scale tubular microbialites. Tubestone microbialites that form in this manner have distinctive and laminated outer walls preserved by mineral precipitation (Fig. 6), and can be locally curved. The parallel laminae in vertical tubes develop in a manner similar to the dense and porous laminae of some predominantly horizontal photosynthetic microbialites (e.g. Monty, 1976). The orientation of filaments in the porous and dense laminae of the horizontal microbialites differs from that in the tubes: the porous laminae in predominantly horizontal microbialites are built by predominantly vertical filaments, while the dense laminae of the horizontal microbialites contain horizontal filaments. The orientation of filaments in the dense and porous laminae in horizontal and vertical microbialites, respectively, is thus a function of the orientation of the initial growth surface, rather than of the direction of light source.

The model of mat growth around photosynthetic bubbles directly applies to the growth of tubular structures with laminated or otherwise distinct walls found within the rock matrix that lacks regular lamination. Some fossil counterparts of these are Upper Cretaceous tubular structures from Tepee Buttes Member of the Pierre Shale Formation in Colorado (Krause *et al.*, 2009) and cm-scale tubestones recognized in the Neorchean Carawine Dolomite (Murphy & Sumner, 2008). The former are described as circular to oval in horizontal cross-section, a few millimeters to tens of millimeters wide and several centimeters to decimeters long, with walls lined with microparticles but not finely laminated (Krause *et al.*, 2009). The marked depletion of ^{13}C in the calcium carbonate minerals precipitated within these tubestones (Krause *et al.*, 2009) is characteristic for carbonate carbon derived from the oxidation of methane. More morphological similarities exist between photosynthetic tubes and Archean tubestones. The latter are described as shallow-water structures 0.4–1.8 cm in diameter that pinch, swell and coalesce along their 10–16 cm length and have mammillate structures on the finely laminated outer walls (Murphy & Sumner, 2008). The formation of tubes by the gas release within modern oxygenic photosynthetic mats is consistent with the inferred shallow-water setting of these Archean tubular structures, but is uncertain in the light of the timing of the evolution of oxygenic photosynthesis. Further studies, including measurements of the carbon isotopic signatures in these structures are needed to test whether the release of methane or oxygenic photosynthesis was responsible in the formation of these centimetric structures. Although tubes forming around gas bubbles have similar scale as the tubular structures commonly found in the Neoproterozoic cap carbonates (Cloud *et al.*, 1974; Corsetti & Grotzinger, 2005) and some younger stromatolites (Lamond & Tapanila, 2003), strong evidence of interactions between growing mats, gas and minerals is missing from the latter structures. The occurrence of Neoproterozoic and younger tubes within regularly laminated stromatolites and their lack of distint walls (Cloud *et al.*, 1974; Lamond & Tapanila, 2003; Corsetti & Grotzinger, 2005) suggests that these tubestones are consistent with the persistence of unusual depressions within stromatolites (Corsetti & Grotzinger, 2005), rather than with the continuous growth of microbial mats around gas bubbles.

CONCLUSIONS

The production of gas within microbial mats can create characteristic preservable morphologies that extend beyond the simple increase in the overall buoyancy of the mat and the stretching of the mat by the underlying gas. Examples of these are sub-mm and mm-scale stable bubbles that form at topographic highs within microbial cones and towers and cm-scale tubes. These structures form when photosynthetic microbial mats generate, colonize and stabilize oxygen-rich bubbles that would otherwise escape to the surrounding liquid or dissolve. Because the stability of photosynthetic bubbles depends both on the mat coverage and the photosynthetic rates, mm-scale heavily covered bubbles are expected to form in deeper water, but a range of sub-mm scale heavily covered stable bubbles or mm-scale partly uncovered stable bubbles can form in shallow water. Cm-scale bubbles can also form, but tend to be unstable, their shape departs from spherical, and they are only partly colonized. Both stable bubbles and photosynthetic tubes can be preserved by the precipitation of minerals within the biomass. Small bubbles are preserved as spherical features surrounded by laminae. The tubes are preserved as structures with thickened walls containing vertical parallel laminae.

Examples of inferred photosynthetic bubbles in fossil microbialites include sub-mm to mm-scale circular structures surrounded by uninterrupted primary laminae at the topographic highs in conical stromatolites. The growth and lithification of cm-scale tubes around unstable bubbles, on the other hand, is a modern-day analog for the development of tubestones within photosynthetic microbial mats as old as Archean. Although oxygen is not the only gaseous metabolite that can form bubbles, it can best explain the presence of gas-influenced primary mat morphologies in fossil microbialites in the absence of characteristic isotopic and morphological signatures associated with cold seeps.

ACKNOWLEDGMENTS

REFERENCES

Bengtson S, Belivanova V, Rasmussen B, Whitehouse M (2009) The controversial ''Cambrian'' fossils of the Vindhyan are real but more than a billion years older. *Proceedings of the National Academy of Sciences of the USA* **106**, 7729–7734.

Bosak T, Liang B, Sim MS, Petroff AP (2009) Morphological record of oxygenic photosynthesis in conical stromatolites. *Proceedings of the National Academy of Sciences of the USA* **106**, 10939–10943.

Campbell SE, Golubic S (1985) Benthic cyanophytes (cyanobacteria) of Solar Lake (Sinai). *Algological Studies* **38/39**, 311–329.

Castenholz RW (1988) Culturing methods for cyanobacteria. In *Methods of Enzymology* (eds Packer L, Glazer AN). Academic Press, San Diego, pp. 68–93.

Chafetz HS, Rush PF, Utech NM (1991) Microenvironmental controls on mineralogy and habit of CaCO^3 precipitates: an example from an active travertine system. *Sedimentology* **38**, 107–126.

Cloud PE Jr, Wright LA, Williams EG, Diehl PE, Walter MR (1974) Giant stromatolites and associated vertical tubes from the Upper Proterozoic Noonday Dolomite, Death Valley region, eastern California. *Geological Society of America Bulletin* **85**, 1869–1882.

Corsetti FA, Grotzinger JP (2005) Origin and significance of tube structures in neoproterozoic post-glacial cap carbonates: example from Noonday Dolomite, Death Valley, United States. *Palaios* **20**, 348–362.

Demicco RV, Hardie LA (1994) *Sedimentary Structures and Early Diagenetic Features of Shallow Marine Carbonate Deposits*. Society of Sedimentary Geology Atlas Series, SEPM, Tulsa, OK, 265 pp.

Donaldson JA (1976) Paleoecology of Conophyton and associated stromatolites in the Precambrian Dismal Lake and Rae Groups. In *Stromatolites. Developments in Sedimentology* (ed. Walter MR). Elsevier Scientific Publishing Company, Amsterdam, pp. 523–534.

Flynn MR, Bush JWM (2008) Underwater breathing: the mechanics of plastron respiration. *Journal of Fluid Mechanics* **608**, 275–296.

Fouke BW, Farmer JD, Des Marais D, Pratt L, Sturchio NC, Burns PC, Discipulo MK (2000) Depositional facies and aqueous-solid geochemistry of travertine-depositing hot springs (Angel Terrace, Mammoth Hot Springs, Yellowstone National Park, U.S.A.). *Journal of Sedimentary Research* **70**, 565–585.

Geankopolis CJ (1993) *Transport Processes and Unit Operations*. Englewood Cliffs, Prentice Hall, NJ.

Gehling JG (2000) Environmental interpretation and a sequence stratigraphic framework for the terminal Proterozoic Ediacara Member within the Rawnsley Quartzite, South Australia. *Precambrian Research* **100**, 65–95.

Gerdes G, Klenke T, Noffke N (2000) Microbial signatures in peritidal siliciclastic sediments: a catalogue. *Sedimentology* **47**, 279–308.

Golubic S (1973) The relationship between blue-green algae and carbonate deposition. In *The Biology of Blue-Green Algae* (eds Carr NG, Whitton BA). Blackwell, Oxford, pp. 434–472.

Hageage GJ, Harrington BJ (1984) Use of Calcofluor white in clinical mycology. *Laboratory Medicine* **15**, 109–112.

Hetsroni G, Mosyak A, Pogrebnyak E, Sher I, Segal Z (2006) Bubble growth in saturated pool boiling in water and surfactant solution. *International Journal of Multiphase Flow* **32**, 159–182.

Hoffman P (1976) Environmental diversity of Middle Precambrian stromatolites. In *Stromatolites* (ed. Walter MR). Elsevier Scientific Publishing Company, Amsterdam, pp. 599–612.

Hughes J, McCully ME (1975) The use of an optical brightener in the study of plant structure. *Stain Technology* **50**, 319–329.

Jahnke LJ, Embaye T, Hope J, Turk KA, Van Zuilen M, Des Marais D, Farmer JD, Summons RE (2004) Lipid biomarker and carbon isotopic signatures for stromatolite-forming, microbial mat communities and Phormidium cultures from Yellowstone National Park. *Geobiology* **2**, 31–47.

Jones B, Renaut RW, Rosen MR (1998) Microbial biofacies in hot-spring sinters: a model based on Ohaaki Pool, North Island, New Zealand. *Journal of Sedimentary Research* **68**, 413–434.

Jorgensen BB, Revsbech NP, Cohen Y (1983) Photosynthesis and structure of benthic microbial mats: microelectrode and SEM studies of four cyanobacterial communities. *Limnology and Oceanography* **28**, 1075–1093.

Krause FF, Clark J, Sayegh SG, Perez RJ (2009) Tube worm fossils or relic methane expulsing conduits? *Palaios* **24**, 41–50.

Lamond RE, Tapanila L (2003) Embedment cavities in lacustrine stromatolites: evidence of animal interactions from Cenozoic carbonates in U.S.A. and Kenya. *Palaios* **18**, 445–453.

McGregor GB, Rasmussen JP (2008) Cyanobacterial composition of microbial mats from an Australian thermal spring: a polyphasic evaluation. *FEMS Microbiology Ecology* **63**, 23–35.

Monty CLV (1976) The origin and development of cryptalgal fabrics. In *Stromatolites* (ed. Walter MR). Elsevier, Amsterdam, pp. 193–250.

Murphy MA, Sumner DY (2008) Tube structures of probable microbial origin in the Neoarchean Carawine Dolomite, Hamersley Basin, Western Australia. *Geobiology* **6**, 83–93.

Noffke N, Gerdes G, Klenke T, Krumbein WE (2001) Microbially induced sedimentary structures: a new category within the classification of primary sedimentary structures. *Journal of Sedimentary Research* **71**, 649–656.

Noffke N, Beukes N, Gutzmer J, Hazen R (2006) Spatial and temporal distribution of microbially induced sedimentary structures: a case study from siliciclastic storm deposits of the 2.9 Ga Witwatersrand Supergroup, South Africa. *Precambrian Research* **146**, 35–44.

Rahn H, Paganelli CV (1968) Gas exchange in gas gills of diving insects. *Respiration Physiology* **5**, 145–164.

Revsbech NP, Jorgensen BB, Blackburn TH, Cohen Y (1983) Microelectrode studies of the photosynthesis and O$_2$, H$_2$S, and pH profiles of a microbial mat. *Limnology and Oceanography* **28**, 1062–1074.

Schieber J, Bose PK, Eriksson PG, Banerjee S, Sarkar S, Altermann W, Catuneanu O (eds)(2007) *Atlas of Microbial Mat Features Preserved Within the Siliciclastic Rock Record Vol 2.* Elsevier, Amsterdam, 324p.

Schultze-Lam S, Ferris FG, SherwoodLollar B, Gerits JP (1996) Ultrastructure and seasonal growth patterns of microbial mats in a temperate climate saline alkaline lake: Goodenough Lake, British Columbia, Canada. *Canadian Journal of Microbiology* **42**, 147–161.

Stueeken EE, Loyd S, Li X, Callow R, de la Torre J, Berelson W, Corsetti F, Hanselmann K, Stevenson BS, Spear J, Pepe-Ranney C, Beer L, Dawson S, Johnson HA (2008) Exploring the role of filamentous cyanobacteria in the formation of living silica stromatolites in yellowstone hot springs, AGU fall meeting. AGU, San Francisco. Abstract B51D-0410.

Thorpe WH, Crisp DJ (1947) Studies on plastron respiration. Part II. The respiratory efficiency of the plastron in Aphelocheirus. *Journal of Experimental Biology* **24**, 270–303.

Vogel S (2006) Living in a physical world {VIII}. Gravity and life in the water. *Journal of Biosciences* **31**, 309–322.

Vopel K, Hawes I (2006) Photosynthetic performance of benthic microbial mats in Lake Hoare, Antarctica. *Limnology and Oceanography* **51**, 1801–1812.

Wharton RA, Parker BC, Simmons GM (1983) Distribution, species composition and morphology of algal mats in Antarctic dry valley lakes. *Phycologia* **22**, 355–365.

Wilson AT (1965) Escape of algae from frozen lakes and ponds. *Ecology* **46**, 376.

APPENDIX

The analysis proceeds along two parallel tracks. In the former case, we apply elementary principles from gas dynamics (Henry's Law, for example) in determining the bubble pressure, p_{bub}. In the latter case, p_{bub} is evaluated from purely mechanical considerations, i.e. from Laplace's equation which relates, through the surface tension, σ, the bubble pressure to the bubble size and, more particularly, to the radius of curvature. A number of simplifying assumptions are documented along the way, chief among them that the system has reached steady state so that the equivalent fraction of the bubble surface covered by bacteria, η, does not vary with time. Relaxation of these assumptions would offer improved insights at the cost of introducing significant complexity. As such, these avenues for model refinement are deferred to future publications.
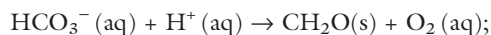
Consideration is restricted to a bubble (i) whose surface forms part of a sphere, and (ii) is enmeshed by a thin film of cyanobacteria. Note that the elastic properties of the biofilm may add an extra tensile strength to the bubble surface beyond that provided by surface tension of water alone. The mechanical properties of cyanobacterial biofilms are poorly documented, and we therefore do not attempt to quantify this added contribution here. In addition, the nucleation of new bubbles on the sides of pre-existing bubbles suggests that the nucleation of bubbles takes place in the presence of a surfactant (Hetsroni *et al.*, 2006) that would decrease σ and thereby counterbalance the influence of the biofilm.

Chemical analysis

We examine oxygenic photosynthetic cyanobacteria that consume HCO_3^- (aq) and produce O_2 (aq) in alkaline solutions where HCO_3^- (aq) is the dominant species of dissolved inorganic carbon. Because of the following reactions associated with photosynthesis:

$$CO_2\,(aq) + H_2O(l) \rightarrow CH_2O(s) + O_2\,(aq);$$

or

$$HCO_3^-\,(aq) + H^+\,(aq) \rightarrow CH_2O(s) + O_2\,(aq);$$

we assume that the local concentrations of dissolved chemical components in regions immediately adjacent to the bacterial film differ from those in the bulk medium. Generically, we write the dissolved gas concentration in the medium and near areas on the outer bubble surface covered by bacteria as x_k and $\underline{x}_k$, respectively. Thus, for example, the local concentration of dissolved O_2, denoted by $\underline{x}O_2$, is expected and observed (data not shown) to be larger than xO_2, the concentration of dissolved O_2 in the surrounding water column. We do not draw a distinction between xN_2 and $\underline{x}N_2$ as we assume that N_2 does not appear as a major reactant or product of light-independent reactions.

The gas-phase chemistry associated with individual bubbles is governed by the three gas component model of Thorpe & Crisp (1947) and Rahn & Paganelli (1968). For each of CO_2, O_2 and N_2, the gas-phase concentration expressed by the partial pressure defined by $p_k = y_k\,p_{bub}$, where y_k is the gas-phase mole fraction of chemical component k, is related to the dissolved gas concentration in the adjoining water phase, i.e.

$$0 = A\eta(\underline{x}O_2 H_{O_2} - pO_2) + A(1-\eta)(xO_2 H_{O_2} - pO_2);\quad (1)$$

$$0 = A\eta(\underline{x}CO_2 H_{CO_2} - pCO_2) + A(1-\eta)(xCO_2 H_{CO_2} - pCO_2);\quad (2)$$

$$0 = A(xN_2 H_{N_2} - pN_2).\quad (3)$$

Here, A is the total surface area of the bubble so that $A\eta$ denotes the equivalent fraction by which biofilm covers the bubble that represents for the number of cells associated with the bubble, either as cells directly on the surface, or cells attached to other cells on the surface of the bubble. H_k is the temperature-dependent Henry's law constant.

Equations (1) and (2) are helpful because they allow us to solve for the local dissolved gas concentrations, $\underline{x}O_2$ and $\underline{x}CO_2$, in terms of the bulk dissolved gas concentrations, xO_2 and xCO_2. We put this information to use below.

Concentration disparities of chemical components between those areas of the bubble surface covered by cyanobacteria and the surrounding water column drive fluxes in the liquid phase, denoted as q_k and expressible as

$$qO_2 = A\eta I_{O_2}(xO_2 - \underline{x}O_2) < 0;\quad (4)$$

$$qCO_2 = A\eta I_{CO_2}(xCO_2 - \underline{x}CO_2) > 0; \quad (5)$$

$$qN_2 = A\eta I_{N_2}(xN_2 - \underline{x}N_2) = 0; \quad (6)$$

$$qHCO_3 = A\eta I_{HCO_3}(xHCO_3^- - \underline{x}HCO_3^-) > 0; \quad (7)$$

$$qH^+ = A\eta I_{H^+}(xH^+ - \underline{x}H^+) > 0, \quad (8)$$

where I_k is a component-dependent liquid-phase mass transfer coefficient (Geankopolis, 1993). Note that a positive flux corresponds to the flow a particular chemical component from the medium to the bubble surface. In contrast to the gas-phase equations (1) through (3), here we also consider a flux of the chemical components HCO_3^- (aq) and H^+ (aq). These chemical components do not appear in the gas phase but they participate in the photosynthetic and water chemistry reactions. Thus, at steady state and assuming that HCO_3^- is the dominant species of inorganic carbon in the medium:

$$-qO_2 = qCO_2 + qHCO_3^-. \quad (9)$$

Moreover,

$$qH^+ = qHCO_3^-. \quad (10)$$

The former constraint describes the net photosynthetic rate (∼10–20% of the gross photosynthetic rate in our experimental system), whereas the latter comes from the requirement that the boundary layer of the bubble cannot, under steady conditions, accumulate a positive or negative electrical charge. The general conclusions of our analysis would hold at higher pH values, where equation (9) is modified to take into account a higher abundance of CO_3^{2-}.

Because $xN_2 = \underline{x}N_2$, equation (6) shows that

$$pN_2 = xN_2 H_{N_2}, \quad (11)$$

while manipulation of equations (4) and (5) to express $\underline{x}_j$ in terms of x_j yields the following expressions for the gas-phase partial pressures of O_2 and CO_2:

$$pO_2 = -\frac{qO_2 H_{O_2}}{A I_{O_2}} + xO_2 H_{O_2}; \quad (12)$$

$$pCO_2 = -\frac{qCO_2 H_{CO_2}}{A I_{CO_2}} + xCO_2 H_{CO_2}. \quad (13)$$

Letting pH_2O denote the partial pressure of water vapor, the bubble pressure is given by:

$$p_{bub} = pH_2O + pCO_2 + pO_2 + pN_2 = pH_2O$$
$$+ x_j H_j - \frac{qO_2 H_{O_2}}{A I_{O_2}} - \frac{qCO_2 H_{CO_2}}{A I_{CO_2}} \quad (14)$$

where, as a shorthand notation, we have set $x_j H_j = xCO_2 H_{CO_2} + xO_2 H_{O_2} + xN_2 H_{N_2}$. From the related analyses of Rahn & Paganelli (1968), Vogel (2006) and Flynn & Bush (2008), we expect that

$$\frac{H_{O_2}}{I_{O_2}} \gg \frac{H_{CO_2}}{I_{CO_2}}$$

owing to the enhanced solubility of CO_2 in water as compared to O_2 and the neutral to alkaline pH of the medium. Equation (14) may be further simplified by writing qO_2 as:

$$qO_2 = -QA\eta,$$

in which Q is the net photosynthetic rate per unit area, giving

$$p_{bub} \cong pH_2O + x_j H_j + \frac{Q\eta H_{O_2}}{I_{O_2}}. \quad (15)$$

Equation (15) shows that the bubble pressure depends on the dissolved gas concentration in the medium and on the rate of O_2 production by cyanobacteria.

Mechanical analysis

Apart from the equation (15), the bubble pressure may also be determined strictly on mechanical grounds by summing the hydrostatic and curvature pressures:

$$p_{bub} = p_{atm} + \rho g H + 2\sigma/R, \quad (16)$$

in which p_{atm} ($<p_{bub}$) is atmospheric pressure, $\rho = 1000$ kg m^{-3} is the water density, $g = 9.8$ m s^{-2} is gravitational acceleration, R is the mean radius of curvature and $H \gg R$ is the water column depth. Equation (16) indicates that larger bubble pressures are associated with smaller radii of curvature, i.e. smaller bubbles whereas smaller bubble pressures are associated with larger radii of curvature, i.e. larger bubbles.

Setting the results of equations (15) and (16) equal to one another shows that

$$pH_2O + x_j H_j - p_{atm} - \rho g H + \frac{Q\eta H_{O_2}}{I_{O_2}} = 2\sigma/R. \quad (17)$$

This simple result offers the following insights:

• When the dissolved gas concentration is relatively low such that p_{atm} is notably larger than $x_j H_j$ (i.e. the medium is strongly sub-saturated), it is difficult to maintain a bubble that is stable against dissolution. Stable bubbles are less likely to form and persist at larger depths where the deleterious impact of light limitation and hydrostatic pressures come into play. An increase of aeration serves to increase $x_j H_j$. In addition, at a higher pCO_2, a higher net flux of oxygen from mats should result in an increase in Q.

• For fixed illumination and dissolved gas concentrations, the volume of photosynthetic bubbles should decrease as more bacteria accumulate along the air–water interface. On the

other hand, for fixed illumination and biofilm density, the mean bubble radius should decrease with increasing aeration of the medium.

• Whereas stable photosynthetic bubbles in shallow, well-illuminated and well-aerated water may be either lightly covered by cyanobacteria and have large radii or heavily covered by cyanobacteria and have smaller radii, bubbles that appear in deeper, less well-illuminated water will tend to be relatively large and inhabited by dense biofilms.

SUPPORTING INFORMATION

Additional Supporting Information may be found in the online version of this article:

Fig. S1 Stable and unstable bubbles at the top of a small photosynthetic tube formed at room temperature at 0 h (beginning of the imaging experiment) and at 29.5 h (the end of the experiment).

Fig. S2 Vertical growth of the mat around photosynthetic bubbles.

Fig. S3 Gas is supplied from the underlying mat to the cm-scale unstable, non-spherical bubbles.

Fig. S4 Calcium carbonate minerals are found in the regions of abundant extra-cellular polymeric substances stainable by Calcofluor White.

Please note: Wiley-Blackwell is not responsible for the content or functionality of any supporting materials supplied by the authors. Any queries (other than missing material) should be directed to the corresponding author for the article.